Alexandria Engineering Journal (2014) 53, 573–582

Alexandria University

Alexandria Engineering Journal

www.elsevier.com/locate/aej
www.sciencedirect.com

ORIGINAL ARTICLE

A bearingless coaxial magnetic gearbox

A.S. Abdel-Khalik [a,*], S. Ahmed [b], A. Massoud [a,c]

[a] Department of Electrical Engineering, Faculty of Engineering, Alexandria University, Alexandria 21544, Egypt
[b] Department of Electrical and Computer Engineering, Texas A&M University at Qatar, 23874, Doha, Qatar
[c] Department of Electrical Engineering, Qatar University, Doha, Qatar

Received 27 November 2013; revised 5 May 2014; accepted 1 June 2014
Available online 28 June 2014

KEYWORDS

Gearbox;
Magnetic planetary gear;
Bearingless machines;
Permanent magnets;
Finite elements;
Speed reduction ratio

Abstract Recently, magnetic gearboxes (MGBs) are serious contenders to their conventional mechanical counterparts in terms of reduced maintenance requirements, improved reliability, tolerance to mechanical inaccuracies, and inherent overload protection. MGBs are preferably employed in high speed applications and compact harsh environments subjected to severe shock and vibration. A high gear ratio MGB is also a suitable candidate for single stage high-speed transmission applications such as helicopter power transmissions. In this paper, the conventional planetary magnetic gearbox is equipped with a three-phase winding to provide additional magnetic levitation capabilities besides torque transmission, thus creating a bearingless MGB configuration. This was achieved by adding a three-phase winding in the space between the ferromagnetic pieces. The current in this additional winding is controlled to provide decoupled axial forces irrespective of the transmitted mechanical power. This feature is important to reduce the mechanical losses especially for high-speed rotors and can be a viable method for vibration suppression.

© 2014 Production and hosting by Elsevier B.V. on behalf of Faculty of Engineering, Alexandria University.

1. Introduction

The magnetic gearbox is a recent technology that offers many advantages over conventional mechanical gearboxes including reduced maintenance and improved reliability, lack of lubrication requirements, precise peak torque transmission, inherent overload protection, physically isolated input and output shafts, misalignment tolerance, and low acoustic noise and vibration [1,2]. In the available literature, different linear and rotary magnetic gear topologies have been investigated [1–8]. One of the promising configurations is the rotary planetary configuration initially proposed in [5]. A detailed comparison between this magnetic gear type and a mechanical planetary gearbox is introduced in [9]. The study shows a comparable performance between the two types with obvious benefits offered by magnetic gearbox inherent in its noncontact magnetic structure. On the other hand, torque density of this configuration falls significantly for gear ratios higher than about 20:1. In [3], a novel magnetic harmonic gearbox, which is similar to a mechanical harmonic gearbox, was introduced to address the higher gear ratio limitations of the planetary magnetic gearbox. An active torque density reaching 150 kN m/m^3 per stage can be achieved when rare-earth permanent magnets are used in this configuration. Moreover,

* Corresponding author. Tel.: +20 1152660227.
E-mail address: ayman@spiretronic.com (A.S. Abdel-Khalik).
Peer review under responsibility of Faculty of Engineering, Alexandria University.

Production and hosting by Elsevier

1110-0168 © 2014 Production and hosting by Elsevier B.V. on behalf of Faculty of Engineering, Alexandria University.
http://dx.doi.org/10.1016/j.aej.2014.06.002

Nomenclature

p	number of pole-pairs
n_s	number of ferromagnetic pole pieces
N	rotor speed (rpm)
ω	rotor angular speed (rad/s)
ω_v	angular frequency of levitation winding current (rad/s)
F	force (N)
B	flux density (T)
R	inner air gap radius (m)
L	gear stack length (m)
μ_0	air permeability (H/m)
θ	air gap peripheral angle (rad)
δ	shift angle between the different flux components
G_r	gear ratio
C_T	cogging torque factor
I	current (A)
J	current density (A/mm^2)
A_s	slot area (mm^2)
a_c	conductor cross-sectional area (mm^2)
A_c	total conductor area (mm^2)
k_{fill}	slot filling factor
T	number of conductors per slot
ϕ	rotor position
x, y	xy radial displacements (m)

Subscript

l	low speed rotor
h	high speed rotor
g	air gap
v	levitation winding
α, β	winding stationary frame

ripple free transmitted torque was obtained. The origin for this cycloid/harmonic gear concept is described in [10]. Despite their advantages, magnetic gears have received minimal industrial attention, mainly due to the perceived initial cost added by permanent magnets. However, their advantages may warrant their application, especially when combined with a high-speed electrical machine resulting in a desirable size/weight and cost effective solution. Hence, MGBs were proposed in applications like wind energy with high-speed generators [11] and contra-rotating tidal turbines [12].

In high-speed electrical machines, the critical speed is a serious problem due to the significant induced vibration on the rotor structure at elevated speeds [13]. The self-bearing or bearingless machine is an electromagnetic device that supports its own rotor by magnetic forces generated from windings on its stator [14]. When compared with conventional active magnetic bearings, bearingless drives offer many advantages which are realized as a result of the integration of a radial magnetic bearing and a motor, including compactness, low cost, and higher power density [15].

The application of bearingless motors in vibration suppression was proven to be effective because the magnetic force is generated within the motor itself [13–15]. The concept of bearingless motors has been developed theoretically in [16]. Since then, the concept has been applied to synchronous reluctance, induction, permanent magnet, disc-type bearingless, homopolar, hybrid, and consequent-pole bearingless drives [17–19]. Bearingless motors are also compatible with the recent trend for miniaturization and the increasing cleanness specifications in chemical, pharmaceutical, biotechnology, and semiconductor industry applications demanding high-purity process environments [20].

In the recent literature, different types of bearingless motors with different winding structures, different converter topologies, and different control methods have been presented to comply with various applications [20–24]. The radial force generated from the bearingless motor has also been used for equipment shaft vibration suppression to go through the first bending critical speed [15,25]. Two kinds of magnetic forces are generated for vibration suppression: spring force, which acts in the opposite direction of the rotor radial displacement, and damping force, which is proportional to the derivative of the negative rotor radial displacement [15,25].

In this paper, the conventional planetary MGB, with a $2p_h$-pole high-speed rotor shown in Fig. 1a is equipped with a $(2p_h - 2)$-pole, 3-phase winding embedded in the space between the ferromagnetic pole-pieces, as shown in Fig. 1 [26,27]. The selected pole-pairs combination between the high-speed rotor and the new levitation winding enables the development of an average unbalanced magnetic pull [17,26]. Hence, the current in this winding can be used to produce controllable radial forces acting on the high speed rotor to provide the MGB with additional magnetic levitation capabilities, emulating a self-aligning bearingless magnetic gearbox.

Mechanical self-aligning bearingless planetary gears (SABP) have been proposed for helicopter applications since the 1960s [28–30]. Many of the advantages that emerged from the use of the mechanical SABP are similar to those generally offered by its magnetic counterpart, such as: eliminating planet bearing power losses and failures, providing sufficient flexibility and self-centering to give good load distribution between planet pinions, effectively isolate planetary elements from housing deflections, and increasing operating time after loss of lubricant. A prototype MGB with the proposed modification is designed based on finite element analysis and simulated to validate the proposed idea [31].

2. Proposed magnetic gearbox

The proposed modifications to a conventional MGB are shown schematically in Fig. 1. The new structure includes a $(2p_h - 2)$-pole levitation winding. A polymer carrier is used to house both the ferromagnetic pole-pieces and the $(2p_h - 2)$-pole three-phase winding. The number of ferromagnetic pole-pieces, n_s, equals the number of both inner and outer magnet pole-pairs, $n_s = p_l + p_h$ [1]. For the magnetic gearbox with a 38/4 ($2p_l/2p_h$) pole combination shown in Fig. 1, the required number of ferromagnetic pole-pieces will be 21. In

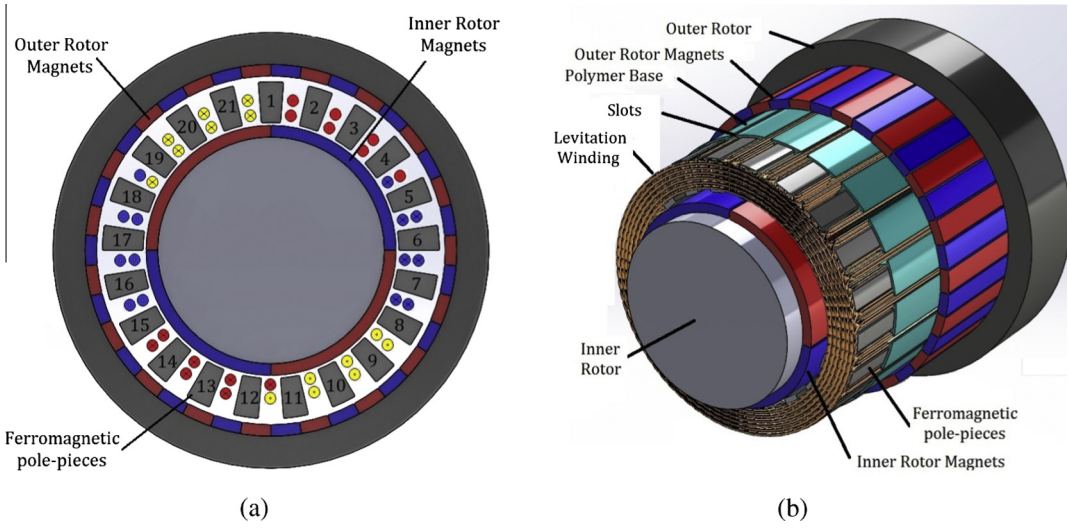

Figure 1 Magnetic planetary gearbox. (a) Cross-sectional view and (b) 3D view.

the following subsections, the principle of radial force generation is presented along with the required pole-pair combination between the high speed rotor magnets and the new levitation winding which produces an average unbalanced magnetic pull in the air gap. It will be shown that for a 4-pole high-speed rotor, the levitation winding should produce a 2-pole flux distribution [17].

2.1. Principal of radial force generation

The cross section of the proposed MGB with the new levitation winding is shown in Fig. 2a. The solid red lines illustrate the flux paths produced by the high speed magnets crossing both the high speed as well as low speed rotors; while the solid blue lines show the flux paths produced by the 2-pole levitation winding.

With the levitation winding current set to zero, the air gap flux density in the inner air gap will be symmetrical and the magnitude of the flux density in the air gap sections 1, 2, 3, and 4 will be the same. Since the attractive force between the rotor poles and the stator iron at any point around the rotor periphery depends on the flux density at this point, the symmetrical flux distribution yields zero average radial force [17].

With the current polarity shown in Fig. 2, and assuming that phase A carries maximum current, another 2-pole flux wave is generated and its direction is as shown in Fig. 2a. In air gap section 1, the flux density increases because the direction of the 4-pole and 2-pole flux is the same. However, in air gap section 3, the flux density decreases because the flux waves are of opposite polarity. The magnetic forces in air gap sections 1 and 3 are no longer equal, i.e., the force in air gap 1 is larger than that in air gap 3. Hence, a radial force $\boldsymbol{F}$ in the positive x-axis direction is produced. The current magnitude and angle control the magnitude and direction of the produced radial force. The concept is quite similar to that of bearingless PM motors [17]. The case when the high speed rotor rotates by 90° is shown in Fig. 2b. To obtain a constant average force in the same positive x-direction, the 2-pole flux should rotate 180° as shown in Fig. 2b. Thus, the angular frequency of the 2-pole winding current should be double the mechanical angular speed of the high speed rotor. Hence, the suspension controller should determine the frequency of

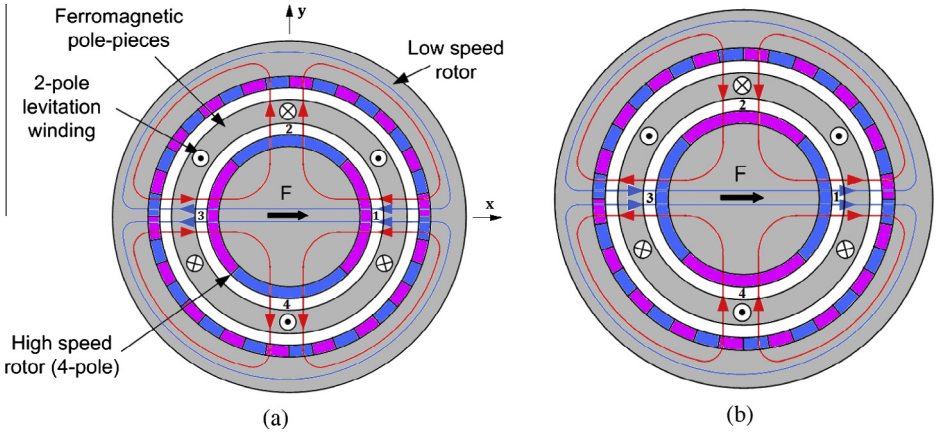

Figure 2 Principle of radial force production (a) $\Phi = 0°$ and (b) $\Phi = 180°$.

the suspension winding current based on the mechanical angular speed of the high speed rotor.

2.2. Unbalanced magnetic pull

Generally, magnetic radial forces are generated in all types of electrical machines due to the radial component of the distributed air gap flux. In machines with a symmetrical winding and constant air gap, the resultant of these distributed radial forces is zero. Unsymmetrical windings or air gap irregularity will give rise to unbalanced magnetic pull. In other words, the resultant forces sum up to a nonzero value [32,33]. It has been shown in the literature that if the machine's air gap flux comprises different flux components with different pole-pairs, radial forces may be generated if and only if the difference between the pole-pairs of these components is one [33].

In a magnetic gearbox, the flux distributions of both inner and outer air gaps contain different flux components with different numbers of pole-pairs. Since the difference between the high speed and low speed rotor pole-pairs is usually more than one, the average force in both inner and outer air gaps adds to zero. Embedding a levitation winding with p_v pole-pairs between the ferromagnetic pole-pieces produces a third field component. Hence, the inner air gap will contain three flux components, namely, the flux produced by the inner magnets with p_h pole-pairs, the flux component produced by the outer magnets with p_l pole-pairs, and the flux component generated from the additional winding with p_v pole-pairs flux distribution. The required relationship between p_v and p_h to obtain a nonzero average radial force is derived using Maxwell's stress method [34]. This method is based on the well-known formula of attraction force between infinitely permeable ferromagnetic surfaces with flux density B_g crossing the air gap surface area A between them. For an infinitesimally small air gap area dA, the radial force is given by Eq. (1).

$$dF = RL\frac{B_g^2}{2\mu_0}d\theta \tag{1}$$

Hence, the horizontal and vertical radial force components exerted due to dA are given by Eqs. (2) and (3).

$$dF_x = RL\frac{B_g^2}{2\mu_0}\cos\theta\ d\theta \tag{2}$$

$$dF_y = RL\frac{B_g^2}{2\mu_0}\sin\theta\ d\theta \tag{3}$$

Radial force components F_x and F_y are given by Eqs. (4) and (5).

$$F_x = RL\int_0^{2\pi}\frac{B_g^2}{2\mu_0}\cos\theta\ d\theta \tag{4}$$

$$F_y = RL\int_0^{2\pi}\frac{B_g^2}{2\mu_0}\sin\theta\ d\theta \tag{5}$$

The flux distribution of inner air gap adjacent to the high speed rotor containing the previously mentioned three flux components can be expressed as using Eq. (6);

$$B_{gh}(\theta,t) = B_{mh}\cos(\omega_h t - p_h\theta + \delta_h) + B_{ml}\cos(\omega_l t - p_l\theta + \delta_l) + B_{mv}\cos(\omega_v t - p_v\theta + \delta_v) \tag{6}$$

where B_{mh}, B_{ml}, and B_{mv} are the flux components in the high speed rotor air gap produced by the inner magnets, outer magnets, and the levitation winding respectively;

$$\omega_h = \frac{2\pi}{60}p_h N_h$$

$$\omega_l = \frac{2\pi}{60}p_l N_l$$

and δ_h, δ_l and δ_v are the relative phase shift angles between the different flux components.

Substituting from Eqs. (6) into Eq. (4), results in the force produced in the inner air gap which is given by Eq. (7).

$$F_{hx} = RL\int_0^{2\pi}\frac{B_{ght}^2(\theta,t)}{2\mu_0}\cos\theta\ d\theta \tag{7}$$

The integral in Eq. (7) has a nonzero value only for $p_v = p_h - 1$ or $p_v = p_l - 1$ [32]. Since p_l is generally larger than p_h and the force component due to the interaction between the inner rotor magnets' flux and the levitation winding flux is of the main interest, the former selection is more practical. Hence, for $p_v = p_h - 1$, the horizontal component of the radial force in the inner air gap is given by Eq. (8). Similarly, the vertical force component is given by Eq. (9).

$$F_{hx}(t) = \frac{\pi RL}{2\mu_0}B_{mh}B_{mv}\cos((\omega_h - \omega_v)t + (\delta_h - \delta_v)) \tag{8}$$

$$F_{hyx}(t) = \frac{\pi RL}{2\mu_0}B_{mh}B_{mv}\sin((\omega_h - \omega_v)t + (\delta_h - \delta_v)) \tag{9}$$

The force components given by Eqs. (8) and (9) will only have constant values if $\omega_v = \omega_h$, which supports the conclusion in the previous subsection. Hence, the force direction can be controlled using the relative current angle δ_v, while the force magnitude can be controlled using the winding current magnitude.

3. Gearbox design

Designing a conventional MGB to obtain a certain transmitted mechanical power at a specific gear ratio is the first step of the process [1,34]. Based on the available slot area, the number of conductors per coil of the added three-phase winding can be selected for a certain value of control current. Hence, the magnitude of the developed radial force depends on the available slot area. If more radial force is needed, an increased winding area would have to be followed by an iterative electromagnetic design to confirm the proper mechanical power throughput.

3.1. Gear ratio design

Generally in magnetic gearboxes, the ferromagnetic pole-pieces are fixed while the inner and outer rotors are rotating in opposite directions. The relationship between the high speed and the low speed rotors is given by Eq. (10), and the corresponding gear ratio is given by Eq. (11)

$$p_h N_h = -p_l N_l \tag{10}$$

$$G_r = \frac{N_h}{N_l} = -\frac{p_l}{p_h} = -\frac{n_s - p_h}{p_h} \tag{11}$$

The selection of the proper combination of pole-pairs for the two rotors to produce a required gear ratio should take into consideration the torque ripples which result on the

rotors. This is especially true on the high-speed rotor, since this may be detrimental to the performance. Torque ripple is caused by the interaction of the rotor permanent magnets with the ferromagnetic pole-pieces, and is generally known as cogging torque [2]. The gear ratio significantly affects the torque ripple magnitude. The cogging torque factor, CT, is defined in [35] to estimate the severity of the torque ripple on performance. The higher this factor, the higher the cogging torque is. This factor is defined using Eq. (12);

$$C_T = \frac{2p_h n_s}{N_c} \tag{12}$$

where N_c is the least common multiple between the number of poles on the high-speed rotor, $2p_h$, and the number of ferromagnetic pole-pieces, n_s. The minimum value for such factor is unity, which constitutes a possible good selection.

The design parameters for the prototype gearbox are given in Table 1. Both the high and low speed rotors are equipped with NdFeB permanent magnets with radial magnetization. The prototype is designed to obtain a gear ratio of 9.5. For the selected 19/2 pole-pairs combination, the required number of pole-pieces is 21. For this pole-pair combination, the cogging torque factor is found to be unity, which is the minimum value for this factor [2]. Hence, a low torque ripple magnitude is expected for this design, as will be shown form the FE simulation.

3.2. Levitation winding design

Based on the selected pole combination, 38/4, a suitable number of pole-pairs for the levitation winding will be 2. The available number of slots will equal the number of ferromagnetic pole pieces, 21. Since the number of slots is odd, a double layer winding is employed with a winding layout shown in Fig. 3, and the location of each coil is shown in Fig. 1a. The number of coils per phase will be 7. The number of turns per coil is determined based on the available slot area, A_s, and the allowable conductor current. Depending on the recommended current density, J, and the maximum conductor current, I, the conductor cross-sectional area is found from Eq. (13).

$$a_c = I/J \tag{13}$$

For a certain fill factor, the conductor area is given by Eq. (14).

$$A_c = k_{fill} A_s \tag{14}$$

Hence, the available number of conductors per slot is given by Eq. (15).

$$T = A_c/a_c \tag{15}$$

Table 1 Parameters of proposed magnetic gear.

Number of pole-pairs on high speed rotor (p_h)	2
Number of pole-pairs on low speed rotor (p_l)	19
Number of stationary ferromagnetic pole-pieces (n_s)	21
Air gap length	1 mm
Inner rotor radius	38 mm
Inner radius of outer rotor	63 mm
Outer radius of outer rotor	75 mm
Inner magnet thickness	5 mm
Outer magnet thickness	3 mm
Stack length	200 mm
Remanence of NdFeB (B_r)	1.03 T
Magnets relative recoil permeability	1.05
Number of conductors per stator slot (T)	50
Conductor cross-sectional diameter	0.6 mm
Control peak current	3 A
Winding current density	5 A/mm^2
Speed of high speed rotor (N_h)	1500 rpm
Speed of low speed rotor (N_l)	157.9 rpm
Inner rotor weight	6.94 kg
Outer rotor weight	7.96 kg
Ferromagnetic pole-pieces weight	3.7 kg
Inner rotor magnet weight	1.95 kg
Outer rotor magnet weight	1.77 kg
Copper weight	1.18 kg
Total weight	23.5 kg
Gear power	3 kW
Maximum radial force	500 N

3.3. Control system configuration

Precise regulation of radial displacement of the high speed rotor requires accurate information on both the magnitude and direction of the air gap flux. Practically, position sensors in both x- and y-directions are used to detect the rotor radial displacements (x and y), while a rotary encoder is used to detect the angular position of the high speed rotor. The required suspension controller will be similar to that of a conventional bearingless PM motor [17] as shown in Fig. 4. The differences between the detected displacements and the commands x^* and y^* are amplified by a PID controller to produce the required suspension winding current components I_x^* and I_y^*. Generally, the high speed rotor radial position commands are set to be the center position in the x- and y-axes, i.e., $x^* = 0$, $y^* = 0$. Hence, the radial suspension current commands are transformed into the radial suspension winding current commands i_α^* and i_β^* based on the rotor angle using Eq. (16).

$$\begin{bmatrix} i_\alpha^* \\ i_\beta^* \end{bmatrix} = \begin{bmatrix} \cos 2\phi & -\sin 2\phi \\ \sin 2\phi & \cos 2\phi \end{bmatrix} \begin{bmatrix} i_x^* \\ i_y^* \end{bmatrix} \tag{16}$$

Eventually, the three-phase currents are determined using a 2-to-3-phase transformation. As depicted from Eq. (16) and shown in Fig. 2, the angular frequency of the suspension winding current is double the mechanical angular speed of the high speed rotor to ensure an average radial force in the required direction.

3.4. MGB with a five-axis active suspension

The previously presented MGB architecture can only provide two-axis magnetic suspension. For a fully levitated system, a five-axis active suspension is employed [17]. Two bearingless units are required in order to generate radial forces in four axes. There is also a thrust magnetic bearing for active axial positioning on the fifth axis. The proposed MGB with a five-axis active suspension is shown in Fig. 5. A conventional mechanical bearing is used on the low speed rotor. Also, four eddy current position sensors for each bearingless unit are used to measure the xy position. The difference between each pair of position sensors in a certain direction gives the rotor displacement in that direction.

Slot Number																				
1	2	3	4	5	6	7	8	9	10	11	12	13	14	15	16	17	18	19	20	21
A	A	A	A	C-	C-	C-	B	B	B	B	A-	A-	A-	C	C	C	C	B-	B-	B-
A	A	A	C-	C-	C-	C-	B	B	B	A-	A-	A-	A-	C	C	C	B-	B-	B-	B-

Figure 3 Suspension winding layout.

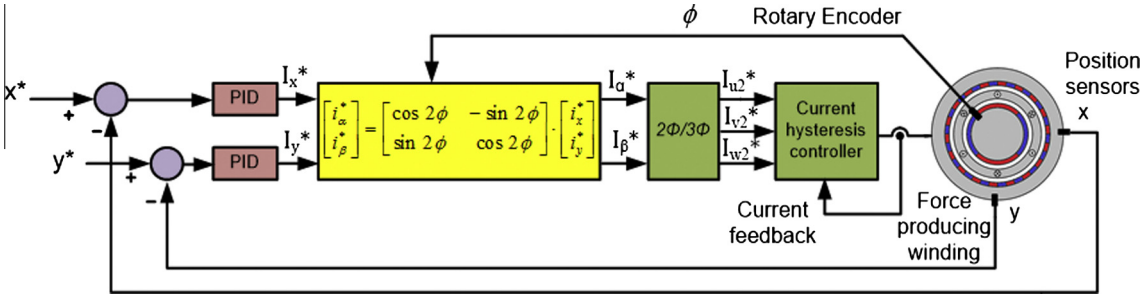

Figure 4 Suspension controller block diagram.

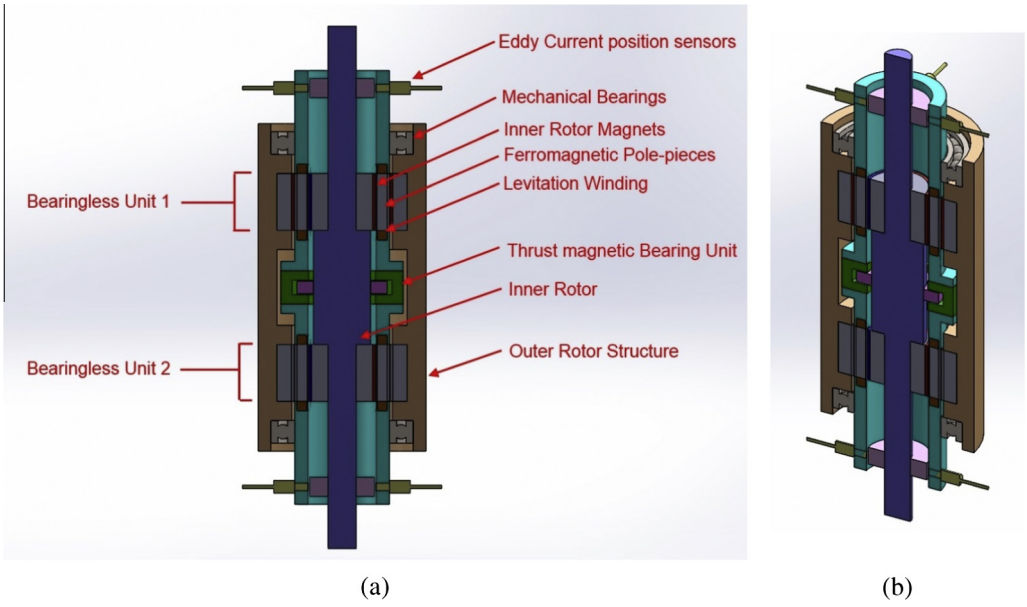

Figure 5 Proposed MGB with Five-axis active suspension. (a) Cross-sectional view and (b) 3D view.

4. Simulation studies

A two-dimensional magneto static finite element method is employed for the simulation studies using JMAG-Studio10. Model parameters are shown in Table 1. The transient module is used to simulate the performance of the proposed bearingless magnetic gear assuming a negligible core loss for simplicity.

4.1. Flux density distribution

The flux density distribution of the proposed gear for two values of the reference *x*-axis current component of the suspension winding, namely 0A and 2A is shown in Fig. 6. It is evident that for I_x equals zero, the flux distribution of the high speed rotor is 4-pole with a symmetrical distribution around the core periphery. However, the 2-pole levitation winding current causes distortion in the flux distribution and a resultant radial force in the positive x direction. It is worthy to mention that the back iron of the low speed rotor should be selected to avoid core saturation with I_x set to its maximum value.

The variation in the radial component of flux density in the air gaps adjacent to the high speed and low speed rotors as well as the flux density in the ferromagnetic pole pieces, corresponding to the high speed and the low speed pole-pair magnets respectively is shown in Fig. 7. It is evident that the two *x*-axis directed north poles in the inner air gap are affected by the suspension winding current as shown in Fig. 7a. The flux density under the first pole, section 1, increases slightly then decreases again under the second pole, section 3. However, the effect on the two south-poles in the *y*-direction,

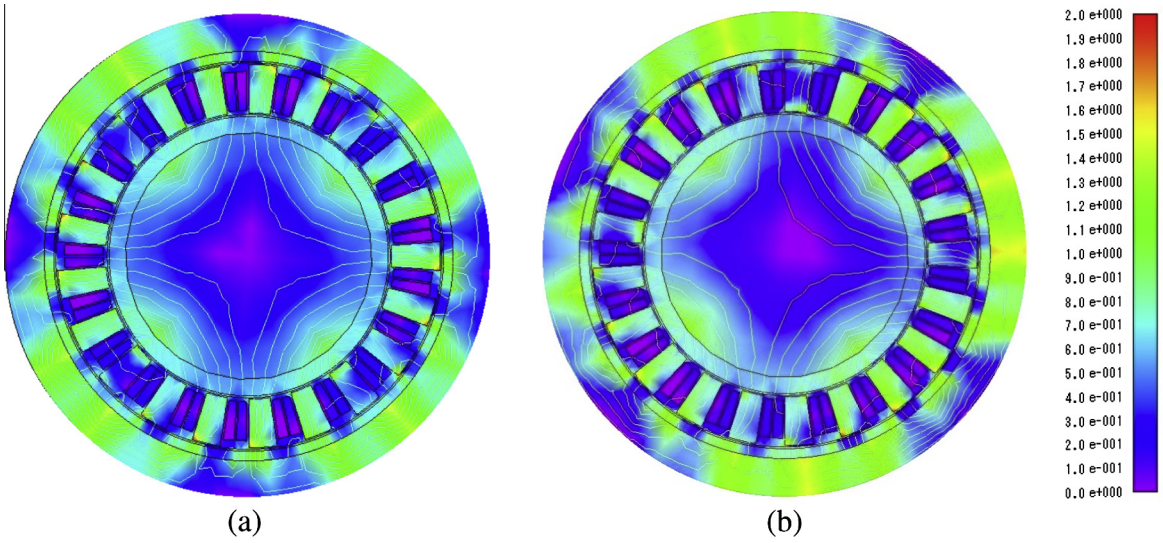

Figure 6 Flux density distribution. (a) $I_x = 0$ and (b) $I_x = 2$A.

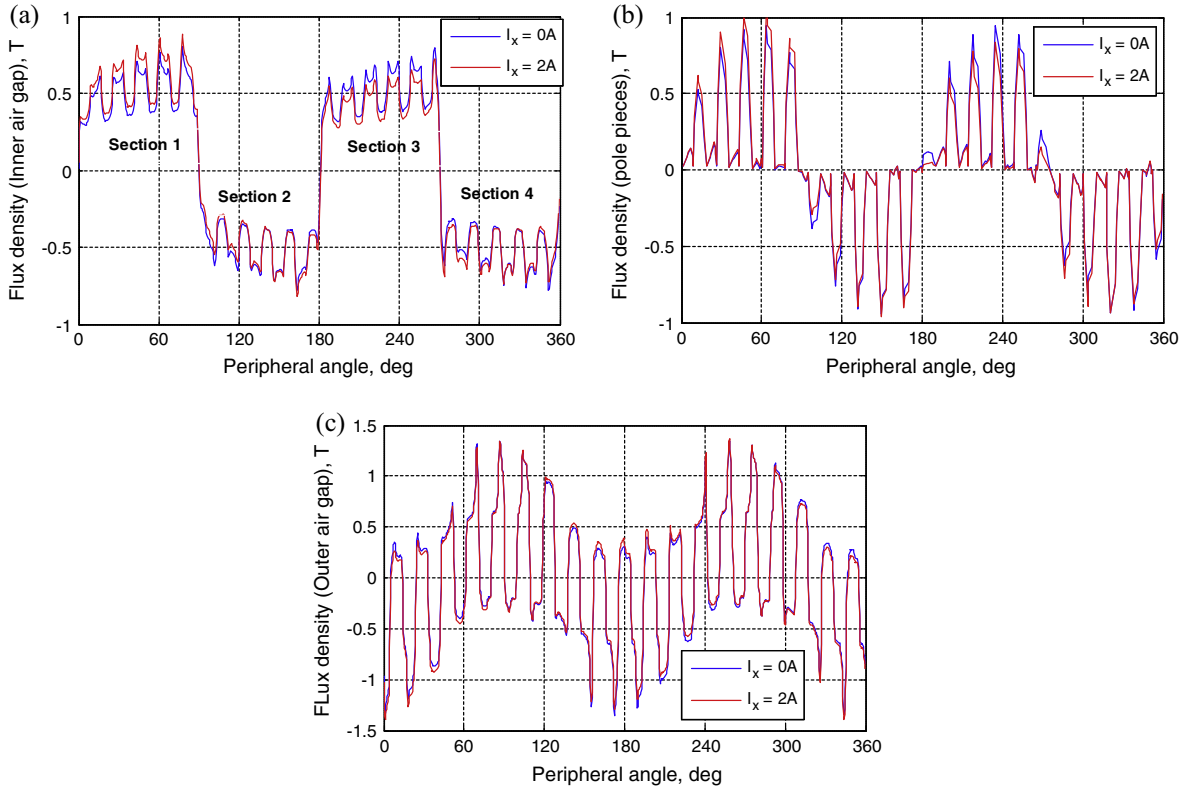

Figure 7 Flux density distribution. (a) Air gap adjacent to high speed rotor. (b) Ferromagnetic pole pieces. (c) Air gap adjacent to low speed rotor.

sections 2 and 4, is neglected. The same effect on the flux density in the ferromagnetic pole pieces is also shown in Fig. 7b. Finally, the effect on the air gap flux of the outer air gap is small, as shown in Fig. 7c.

4.2. Torque transmission

In this subsection, the torques on the low speed and high speed rotors are simulated for the same values of I_x, namely 0A and 2A. The high speed rotor is assumed to rotate at 1500 rpm. Hence, the low speed rotor will rotate in the opposite direction at 157.9 rpm, as given by Table 1. Therefore, for each complete cycle of the low speed rotor, the high speed rotor rotates 9.5 complete cycles in the opposite direction. Maximum load angle between the two rotors is assumed in the two cases, which corresponds to maximum output torque and is determined as in [11]. The torque of both low speed and high speed rotors for the two cases is shown in Fig. 8. It is evident that the effect

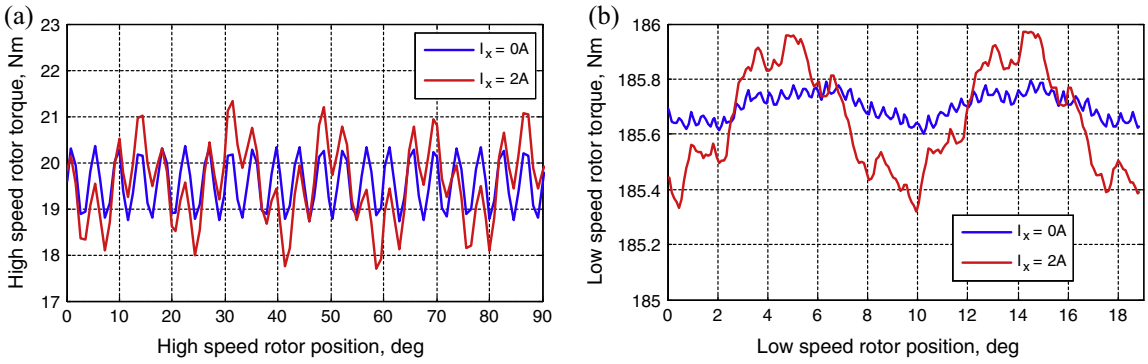

Figure 8 Transmitted mechanical torque for different suspension current component I_x. (a) High speed rotor and (b) low speed rotor.

of suspension winding current on torque production is neglected which ensures decoupling between torque and force generation. On the other hand, the torque ripples slightly increase with the increase of I_x.

4.3. Radial suspension force generation

Simulation results for the radial forces exerted on both high speed and low speed rotors and for the same two values of I_x are shown in Figs. 9 and 10 respectively. The xy components of the radial forces with zero suspension winding current are shown in Figs. 9a and 10a. Despite the relatively high magnitude of the oscillating components of the instantaneous radial forces, it is notable that the average values of these forces equals zero. This oscillatory component of the radial force is mainly due to slotting effect [36] and the corresponding oscillation frequency depends on the number of ferromagnetic pole pieces. With I_x is set to 2A, an average radial force component of 340 N exerted on the high speed rotor in the x-axis direction is generated, while the average force in the y-direction still zero, as shown in Fig. 9b. For the low speed rotor, a corresponding x-component of the radial force and a small y-component are generated, as shown in Fig. 10b. Since, the control and the required magnetic levitation capabilities are related to the high speed rotor only, the forces induced on the low speed rotor are not important since the low speed rotor utilizes a normal mechanical bearing.

A relationship between the I_x component and the corresponding generated radial force on the high speed rotor is plotted in Fig. 11a. For the designed gear, approximately 500 N of radial force can be produced. This value of radial force is a design dependent factor that depends on mechanical design requirements. Changing this value would necessitate another electromagnetic FE design iteration to increase the available slot area to increase the number of turns of the levitation winding and hence the generated radial force.

Finally, the unbalance pull force, which represents a relationship between the generated radial force and the radial displacement, is calculated. The unbalance pull force is important because it is the cause of inherently unstable characteristics for magnetic suspension systems. This relationship is found by introducing a certain radial displacement in the axis of rotation of the high speed rotor with the winding suspension current set to zero. FEA is then used to calculate the average induced pull force caused by this eccentricity. This relationship is plotted in Fig. 11b. This relationship is approximately linear and its slope is called the force–displacement factor, which represents the system static stiffness. Because this factor is positive, generally, magnetic bearings are inherently unstable. Therefore there is a requirement to provide enough negative position feedback to cancel the effect of this coefficient, which is usually done by employing a derivative controller as shown in the controller block diagram given in Fig. 4 [17]. Hence, the radial force generated for the prototype machine as a function of both I_x and radial displacement x can be approximated by Eq. (17).

$$F_x\ (\mathrm{N}) = 169 I_x\ (\mathrm{A}) + 160x\ (\mathrm{mm}) \tag{17}$$

The current and displacement constants in Eq. (17) are used to design the required PID controller shown in Fig. 4. The PID

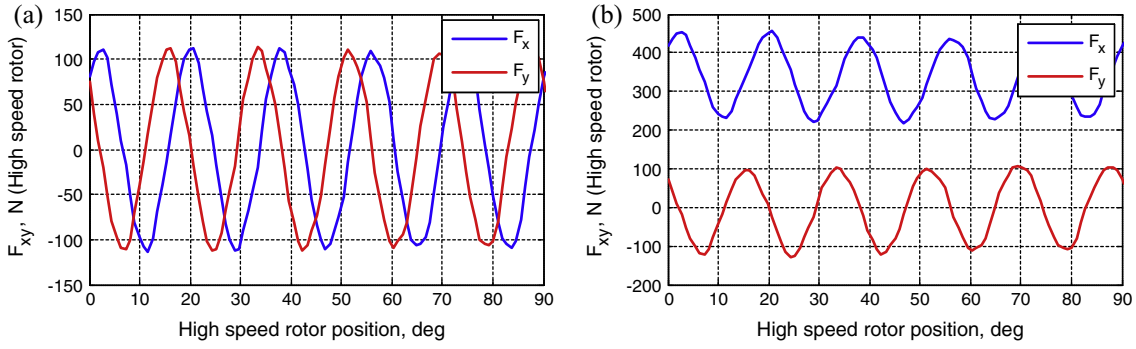

Figure 9 Radial force on high speed rotor. (a) $I_x = 0$ A and (b) $I_x = 2$ A.

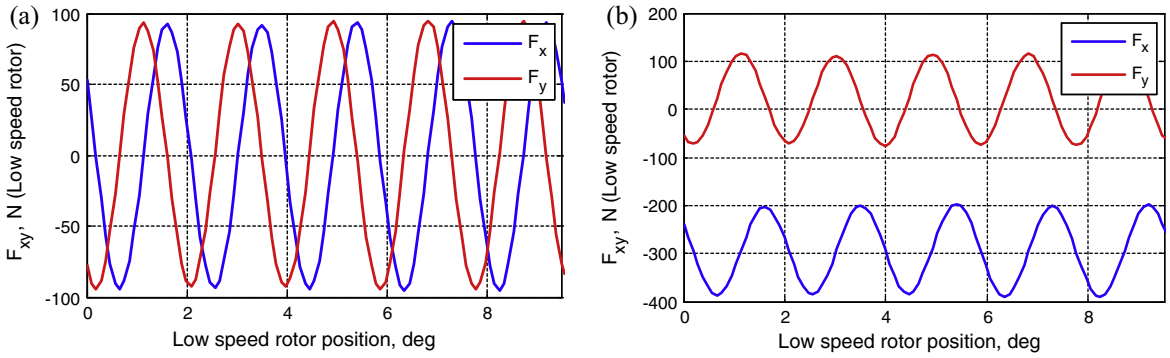

Figure 10 Radial force on high speed rotor. (a) $I_x = 0$ A and (b) $I_x = 2$ A.

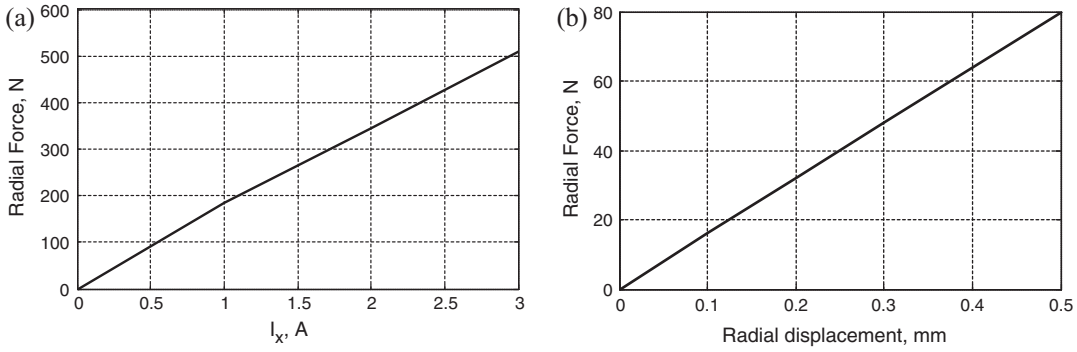

Figure 11 (a) Relationship between I_x current component and radial force and (b) relationship between radial displacement and radial force generated in high speed rotor (static stiffness).

controller design is out of scope of this paper and is similar to that of conventional bearingless PM motors [17,25].

5. Conclusion

A magnetic planetary gearbox with magnetic suspension is introduced in this paper. If the number of pole-pairs of the high speed rotor is p_h, then the ferromagnetic pole-pieces in the conventional MGB are simply equipped with a $p_h - 1$ pole-pairs three-phase winding. By controlling the current in this additional winding, a controllable radial force is introduced on the high speed shaft of the MGB which can then be used for magnetic levitation. This configuration can be also used for vibration suppression. A prototype 3 kW gearbox with a gear ratio of 9.5 is designed and simulated using a finite element package. The simulation of the designed gearbox reveals that the added suspension winding does not affect torque transmission, does not affect the gearbox's performance in terms of induced torque ripple due to the cogging effect, and a complete decoupling between torque and radial force generation is obtained. Helicopter power transmissions are a good application for such a system. Such transmissions are preferably self-aligning such that a shaft can be supported without bearings and is operably coupled to another shaft. Experimental verification of a scaled version of the proposed concept for a helicopter power transmission is planned as a future activity.

Acknowledgment

This publication was made possible by NPRP Grant NPRP 4 - 941 - 2 - 356 from the Qatar National Research Fund (a member of Qatar Foundation). The statements made herein are solely the responsibility of the authors.

References

[1] K. Atallah, S.D. Calverley, D. Howe, Design, analysis and realization of a high-performance magnetic gear, Proc. Inst. Elect. Eng. – Electric Power Appl. 151 (2) (2004) 135–143.
[2] P.O. Rasmussen, T.O. Andersen, F.T. Jorgensen, O. Nielsen, Development of a high performance magnetic gear, IEEE Trans. Ind. Appl. 41 (3) (2005) 764–770.
[3] J. Rens, K. Atallah, S.D. Calverley, D. Howe, A novel magnetic harmonic gear, IEEE Trans. Ind. Appl. 46 (1) (2010) 206–212.
[4] R. Holehouse, K. Atallah, J. Wang, Design and realization of a linear magnetic gear, IEEE Trans. Magn. 47 (10) (2011) 4171–4174.
[5] K. Atallah, D. Howe, A novel high-performance magnetic gear, IEEE Trans. Magn. 37 (4) (2001) 2844–2846.
[6] Ryan Montague, Chris Bingham, Kais Atallah, Servo control of magnetic gears, IEEE/ASME Trans. Mechatron. 17 (2) (2012) 269–278.
[7] Ryan Montague, Chris Bingham, Kais Atallah, Magnetic gear pole-slip prevention using explicit model predictive control, IEEE/ASME Trans. Mechatron. 18 (5) (2013) 1535–1543.

[8] Mi-Ching Tsai, Cheng-Chi Huang, Development of a variable-inertia device with a magnetic planetary gearbox, IEEE/ASME Trans. Mechatron. 16 (6) (2011) 1120–1128.
[9] E. Gouda, S. Mezani, L. Baghli, A. Rezzoug, Comparative study between mechanical and magnetic planetary gears, IEEE Trans. Magn. 47 (2) (2011) 439–450.
[10] F. Jørgensen, T. Andersen, P. Rasmussen, The cycloid permanent magnetic gear, IEEE Trans. Ind. Appl. 44 (6) (2008) 1659–1665.
[11] N.W. Frank, H. Toliyat, Gearing ratios of a magnetic gear for wind turbines, in: Conf. IEMDC, 2009, pp. 1224–1230.
[12] L. Shah, A. Cruden, B.W. Williams, A variable speed magnetic gear box using contra-rotating input shafts, IEEE Trans. Magn. 47 (2) (2011) 439–450.
[13] A. Chiba, K. Sotome, Y. Iiyama, M. Azizur Rahman, A novel middle-point-current-injection-type bearingless PM synchronous motor for vibration suppression, IEEE Trans. Ind. Appl. 47 (4) (2011) 1700–1706.
[14] Jiancheng Fang, Shiqiang Zheng, Bangcheng Han, AMB vibration control for structural resonance of double-gimbal control moment gyro with high-speed magnetically suspended rotor, IEEE/ASME Trans. Mechatron. 18 (1) (2013) 32–43.
[15] E. Simon Mushi, Zongli Lin, E. Paul Allaire, Design, construction, and modeling of a flexible rotor active magnetic bearing test rig, IEEE/ASME Trans. Mechatron. 17 (6) (2012) 1170–1182.
[16] A. Chiba, T. Deido, T. Fukao, M.A. Rahman,, An analysis of bearingless AC motors, IEEE Trans. Energy Convers. 9 (1) (1994) 61–68.
[17] A. Chiba, T. Fukao, O. Ichikawa, M. Oshima, M. Takemoto, D. Dorrell, Magnetic Bearings and Bearingless Drives, Newnes, An Imprint of Elsevier, 2005.
[18] J. Asama et al, Evaluation of a bearingless PM motor with wide magnetic gaps, IEEE Trans. Energy Convers. 25 (4) (2010) 957–964.
[19] Y. Asano et al, Development of a four-axis actively controlled consequent-pole-type bearingless motor, IEEE Trans. Ind. Appl. 45 (4) (2009) 1378–1386.
[20] T. Nussbaumer, P. Karutz, F. Zurcher, J.W. Kolar, Magnetically levitated slice motors—an overview, IEEE Trans. Ind. Appl. 47 (2) (2011) 754–766.
[21] B. Warberger, R. Kaelin, T. Nussbaumer, J.W. Kolar, 50 Nm / 2500 W bearingless motor for high-purity pharmaceutical mixing, IEEE Trans. Industr. Electron. 59 (5) (2012) 2236–2247.
[22] L. Chen, W. Hofmann, Speed regulation technique of one bearingless 8/6 switched reluctance motor with simpler single, IEEE Trans. Industr. Electron. 59 (6) (2012) 2592–2600.
[23] X.L. Wang, Q.-C. Zhong, Z.Q. Deng, S.Z. Yue, Current-controlled multi-phase slice permanent magnetic bearingless motors with open-circuited phases: fault-tolerant controllability and its verification, IEEE Trans. Industr. Electron. 5 (5) (2012) 2059–2072.
[24] T. Reichert, T. Nussbaumer, J.W. Kolar, Bearingless 300-W PMSM for bioreactor mixing, IEEE Trans. Industr. Electron. 59 (3) (2012) 1376–1388.
[25] A. Chiba, T. Fukao, M. Azizur Rahman, Vibration suppression of a flexible shaft with a simplified bearingless induction motor drive, IEEE Trans. Ind. Appl. 44 (3) (2008) 745–752.
[26] A.S. Abdel-Khalik, A. Massoud, A. Elserougi, S. Ahmed. A coaxial magnetic gearbox with magnetic levitation capabilities, in: Conf. ICEM, 2012, pp. 542–548.
[27] A.S. Abdel-Khalik, S. Ahmed, A. Massoud, A. Elserougi, Magnetic gearbox with an electric power output port and fixed speed ratio for wind energy applications, in: Conf. ICEM, 2012, pp. 702–708.
[28] J.G. Kish, Small-size High-speed Transmission System for Use in Microturbine-powered Aircraft, U.S. Patent 7 481 396 B2, 2009.
[29] D. J. Folenta, Design Study of Self-aligning Bearingless Planetary Gear (SABP), NASA Report, 1983.
[30] D. Folenta, W. Lebo, Design, manufacture, and spin test of high contact ratio helicopter transmission utilization self-aligning bearingless planetary (SABP), NASA Technical Report 88-C-009, 1988.
[31] A. Abdel-Khalik, A. Massoud, A. Elserougi, S. Ahmed, A Coaxial Magnetic Gearbox with Magnetic Levitation Capabilities, in Conf, ICEM (2012) 542–548.
[32] L. Wang, R.W. Cheung, Z. Ma, J. Ruan, Y. Peng, Finite-element analysis of unbalanced magnetic pull in a large hydro-generator under practical operations, IEEE Trans. Magn. 44 (6) (2008) 1558–1561.
[33] D.G. Dorrell, A.M. Knight, R.E. Betz, Issues with the design of brushless doubly-fed reluctance machines: unbalanced magnetic pull, skew and iron losses, in Conf, IEMDC (2011) 663–668.
[34] Z.Q. Zhu, D. Ishak, D. Howe, J. Chen, Unbalanced magnetic forces in permanent-magnet brushless machines with diametrically asymmetric phase windings, IEEE Trans. Ind. Appl. 43 (6) (2007) 1544–1553.
[35] Z.Q. Zhu, D. Howe, Influence of design parameters on cogging torque in permanent magnet machines, IEEE Trans. Energy Convers. 15 (5) (2000) 407–412.
[36] D. Žarko, D. Ban, I. Vazdar, Vladimir Jarić, Calculation of unbalanced magnetic pull in a salient-pole synchronous generator using finite-element method and measured shaft orbit, IEEE Trans. Ind. Electron. 59 (6) (2012) 2536–2549.